applied optics

Nested Sampling aided determination of tantalum optical constants in the EUV spectral range

Qais Saadeh,[1,*] Philipp Naujok,[2] Meiyi Wu,[3] Vicky Philipsen,[3] Devesh Thakare,[3] Frank Scholze,[1] Christian Buchholz,[1] Christian Stadelhoff,[1] Thomas Wiesner,[1] and Victor Soltwisch[1]

[1]Physikalisch-Technische Bundesanstalt (PTB), Abbestraße 2-12, 10587 Berlin, Germany
[2]OptiX fab GmbH, Otto-Schott-Str. 41, 07745 Jena, Germany
[3]Imec, Kapeldreef 75, B-3001 Leuven, Belgium
*Corresponding author: qais.saadeh@ptb.de

Received 9 August 2022; revised 18 October 2022; accepted 19 October 2022; posted 19 October 2022; published 17 November 2022

We report on determining the optical constants of Ta in the sub-extreme ultraviolet (EUV) spectral range 5.0–24.0 nm from the angle-dependent reflectance (ADR) measured using monochromatized synchrotron radiation. Two sputtered samples with differing thicknesses were investigated. Complementarily x-ray reflectance was measured at shorter wavelengths and evaluated by Fourier transform to facilitate an unambiguous selection of a model for the data evaluation based on an inverse solution of the Fresnel's equations for a layered system. Bayesian inferences coupled with a Nested Sampling (NS) algorithm were utilized to derive the optical constants with their corresponding uncertainties. This report further emphasizes the applicability of an acclaimed NS algorithm on a high-dimensional inverse problem. We explore the possibility of addressing the correlations between the optical constants of thin films and their structural parameters based on other established studies. © 2022 Optica Publishing Group under the terms of the Optica Open Access Publishing Agreement

https://doi.org/10.1364/AO.472556

1. INTRODUCTION

The year 2019 saw extreme ultraviolet lithography (EUVL) systems using extreme ultraviolet (EUV) radiation, and managing high-volume manufacturing (HVM) standards [1,2]. The shift to EUVL utilizing a wavelength of 13.5 nm opened wider possibilities for the integrated circuit (IC) industry. Meanwhile, optical components and photoresists have been studied to examine the potential applicability of a wavelength in the vicinity of 6.5 nm for the so-called "beyond EUVL" (BEUVL) [3–5]. The applications of EUV radiation surpass lithography; they span EUV astronomy (EUVA) [6], *in situ* imaging and microscopy [7–9], ptychography [10], and surface modification [11]. All the aforementioned applications require accurate optical data, where designing any optical component requires knowledge of the optical constants of its constituents.

In the soft x-ray and EUV spectral ranges, the optical constants are usually given as dependencies of the wavelength as denoted by the complex index of refraction $\bar{n}$: ($\bar{n}(\lambda) = 1 - \delta(\lambda) + i\beta(\lambda)$. At a given wavelength λ , considering an electromagnetic wave, the real part of complex index of refraction $1 - \delta(\lambda)$ is known as the refractive index and relates to the phase velocity, while the imaginary part $\beta(\lambda)$ is known as the extinction coefficient and relates to the absorption. For many elements that are pertinent to EUV-based technologies, there have been significant inconsistencies in the reported optical constants regarding different sources. Zr, Co, and Mo are examples [12–14]. There are various explanations for such significant differences, but for most materials these differences have not been explained. Even for some highly chemically stable and oxidation resistant materials, significant differences were found as in the case of Pt [15]. Such issues motivate a comprehensive effort to examine the optical constants, especially for promising optical materials. Relevant discussions on the discrepancies found regarding different sources are available in [14,16].

For EUV photomasks, Mo/Si multilayer mirrors (MLMs) with Ta-based absorber layers are widely used. Ta is known for its chemical stability, corrosion resistance, and high extinction coefficient in the EUV. Etching processes of Ta-based absorbers would not severely degrade its reflectance [17]. Known from proximity x-ray lithography, Ta absorbers are known for their good pattern ability and relatively low lattice stresses [18]. These traits have given Ta considerable attention. $TaTe_2O_7$ films were reported for their potential applicability as an alternative for known TaN absorbers [19]. Concerning our recent work, some Ta-Ru and Ta-Co binary alloys were found promising in partially mitigating the so-called "3D mask effects" of absorber layers intended for high-numerical aperture (NA) EUVL scanners [20,21].

Optical constants are usually determined either using angle-dependent reflectance (ADR) or transmission-mode measurements (TMM) in the EUV spectral range. Numerous other methods can be also used [22–25] (reviews are available elsewhere [13,26–29]). However, for TMM, thin standing films are usually needed, and only the extinction coefficients are measured experimentally. The refractive indices are calculated using Kramer–Kronig analysis, and this optimally requires extinction coefficients measured through the entire electromagnetic spectrum. However, ADR offers an option enabling the simultaneous determination of two parts of the complex refractive index, at any wavelength. ADR is preferred here since it better supports the so-called "at-wavelength metrology" approach [30].

Determining optical constants from ADR is challenged with a high-dimensional and, most likely, multimodal inverse problem. This is the main disadvantage of ADR as a method for determining optical constants. Adding to the challenge, classical optimization methods do not normally retrieve the correlations and uncertainties of the problem's parameters. Most classical optimization methods merely yield best-fits for the targeted parameters. Also, since ADR solution space is complex and likely multimodal, classical optimization methods are also vulnerable to local minima bias [31]; hence, they are deemed suboptimal in many cases. To mitigate some of the aforementioned limitations, Bayesian-based inferences can be used. Bayesian-based inferences can be classified either as parameter-estimation or model-selection methods [32]. The former class, to which Markov chain Monte Carlo (MCMC) based Bayesian inferences belongs, proved to be a capable formalism in treating highly dimensional problems [33]. In the Physikalisch-Technische Bundesanstalt (PTB), MCMC-based Bayesian inferences have been used in treating ADR targeting optical constants determination [13,34–36]. However, MCMC-based Bayesian inferences have a prime limitation since they do not automatically calculate the evidence of the inverse-problem [37,38]. Also, the convergence diagnostics are often not well-defined [38], and many of them are not straightforward (see [39]). Moreover, depending on the problem, MCMC methods can be inefficient in treating highly degenerate parameter spaces [32]. Arguably, the aforementioned issues, among others, can be alleviated using a model selection class Bayesian method, i.e., nested sampling (NS) [37,38]. NS was proposed in 2004 by Skilling as a Monte Carlo algorithm to calculate the evidence while delivering the posterior distribution consequentially [37,40]. The value of the estimated evidence serves as a robust stopping criterion for the sampling process, as it aids model selection in highly degenerate posteriors [32,38]. A prime aspect of our work is further demonstrating the applicability of a NS algorithm in treating ADR for the determination of optical constants in the EUV spectral range.

Recently, NS has been successfully utilized to infer statistical information in many fields, such as the pharmaceutical industry [41], potential energy surfaces studies [42], and most notably astronomy. Generally, every inferences (or optimization) method has its own advantages and drawbacks [38,43]. Thus, for the EUV community, it is quite handy to establish as many additional computational approaches aiding in the determination of optical constants using ADR. Also, NS is receiving substantial developments; for example, variants such as diffusive nested sampling have been implemented [43]. Widening the user community of a computational approach automatically assist its further development.

In our work, the optical constants are determined in the spectral range 5.0–24.0 nm (ca. 250–ca. 52 eV). Also, we report on examining the potential correlation between the optical constants of Ta thin films and their thicknesses, since two samples with differing thicknesses (30 and 50 nm) were characterized. The optical constants of Ta in the EUV spectral range have been investigated [44–49]. Of the aforementioned references, only Windt *et al*. [48] provided uncertainties for their tabulations; however, merely four points were measured between 5.0 and 24.0 nm in the latter work. Here, the fine-structure is properly sampled, the uncertainties, and the correlations of the inverse-problem free parameters are retrieved. Our results are compared with five published data sets [44–48,50].

2. EXPERIMENTAL METHODS

A. Samples Preparation

The two samples were fabricated using direct current (DC) magnetron sputtering. The substrates were super-polished 300 mm Si wafers. After evacuating the sputtering chamber to a pressure level below 10^{-7} mbar, highly pure Ar gas was purged. The two examined samples here are square coupons each with a side length of 25 mm, cleaved from the sputtered 300 mm Si wafers. Additional details on the sputtering process can be found in [51].

The nominal thicknesses for the two samples were 30.0 and 50.0 nm; throughout this report, these samples will be denoted as Sample 30 and Sample 50, respectively.

B. Reflectivity Measurements

To enable the determination of optical constants using ADR, extreme-ultraviolet reflectance (EUVR) profiles in the spectral range 5.0–24.0 nm were collected. The data acquisition was carried out at the soft x-ray radiometry beamline (SX700) in the radiometry laboratory of the PTB, in the electron storage facility BESSY II of Helmholtz Centre for Materials and Energy (HZB) [52–54].

The S -polarized EUVR of Sample 30 and Sample 50 was measured in the spectral ranges of 5.0–24.0 and 10.0–20.0 nm, respectively. The EUVR of Sample 30 was measured regarding the angular range 3.0°–85.5°, where Sample 50 was measured regarding 4.5°–87.0°. For both samples, the wavelength increment and the angular step were 0.25 nm and 1.5°, respectively.

Furthermore, to assist in reconstructing a model for the relevant EUVR inverse-problems, x-ray reflectance (XRR) profiles were taken from Sample 30 and from a twin sample of Sample 50 at $\mathrm{Cu}-\mathrm{K}\alpha$ in the in the laboratories of OptiX fab GmbH and imec. Sample 50 and its twin were realized using the same, nominal, deposition settings.

3. NESTED SAMPLING BAYESIAN INFERENCES AND MODEL SELECTION

To retrieve the optical constants with their correlations and the uncertainties (among other parameters) from the collected EUVR data, the inferences problem can be formulated given Bayes' theorem as [36]:

$$\Pr(\boldsymbol{p}|\boldsymbol{R}_{\text{measured}}) = \frac{\Pr(\boldsymbol{R}_{\text{measured}}|\boldsymbol{p})\ \Pr(\boldsymbol{p})}{\Pr(\boldsymbol{R}_{\text{measured}})}. \tag{1}$$

Here, $\boldsymbol{p}$ denotes the ensemble of parameters to be determined given the measured EUVR ($\boldsymbol{R}_{\text{measured}}$) from an assumed model. $\Pr(\boldsymbol{p}|\boldsymbol{R}_{\text{measured}})$ is the posterior distribution quantifying the probability of the ensemble $\boldsymbol{p}$ to stand for the measured EUVR. $\Pr(\boldsymbol{R}_{\text{measured}}|\boldsymbol{p})$ is the likelihood function, which indicates the *fitness* regarding the measured against the simulated EUVR based on the information content of the prior knowledge about the sample. For a number (n) of measured points and corresponding absolute uncertainties (σ), the likelihood is in our case formulated as [36]:

$$\Pr(\boldsymbol{R}_{\text{measured}}|\boldsymbol{p}) = \prod_n \frac{1}{\sqrt{2\pi\sigma_n{}^2}} \times \exp\left[-\frac{\left(R_{\text{simulated},\,n}(\boldsymbol{p}) - R_{\text{measured},\,n}\right)^2}{2\,\sigma_n{}^2}\right], \tag{2}$$

where $\Pr(\boldsymbol{p})$ is the prior knowledge, which reflects our beliefs about the sample and the targeted ensemble $\boldsymbol{p}$. The prior knowledge is named as it contains information that is known *a priori*, even before collected the data. $\Pr(\boldsymbol{R}_{\text{measured}})$ is the evidence (also known as the marginal likelihood or the integrated likelihood), and this particular normalizing factor is the target of NS [55]. In the parameter-estimation methods, such as the MCMC Bayesian-based inferences, the evidence is often omitted from Eq. (1), and the posterior distribution is given as a proportionality to the product of the likelihood and the prior distributions [32].

For a more concise notation, Eq. (1) can be rewritten as:

$$P(\theta) = \frac{L(\theta)\,\pi(\theta)}{Z}, \tag{3}$$

where θ denotes the parameters of the model. The evidence Z is basically and integral, and it can be written as:

$$Z = \int_{\Theta} L(\theta)\ \pi(\theta)\ \mathrm{d}^n\theta. \tag{4}$$

Calculating the n -dimensional integral of Eq. (4) can be facilitated where it can be transformed to a single-dimension integration problem [40]. That is, upon partitioning the prior volume, denoted $\mathrm{X}(\theta)$ so that $d\mathrm{X}(\theta)$ equals $\pi(\theta)\,d^n\theta$, Eq. (4) becomes [38,40]:

$$Z = \int_0^1 L(\theta)\ \mathrm{dX}(\theta)\,. \tag{5}$$

Then, Eq. (5) can be estimated using a series:

$$Z \approx \sum_i^N L_i\, w_i. \tag{6}$$

N is the number of points to be sampled, w_i denotes the weight with the i th point and is given by:

$$w_i = \frac{X_{i-1} - X_i}{2}. \tag{7}$$

The numerator of Eq. (7) is the residual regarding the segment of the prior volume constrained between the projected iso-contour lines of the likelihood from L_i through L_{i-1} [56]. The NS core value is in estimating the summation of Eq. (6); details on the relevant statistical evaluation are explained elsewhere [55].

The evidence is crucial when judging between two rival models. In other words, if there existed two different models with identical priors describing our sample, then the known Bayes' factor (BF) given by [57]:

$$BF_{1,\ 2} = \frac{Z_1}{Z_2} \tag{8}$$

could provide a criterion where an increasing $BF_{1,\,2}$ indicates that Model 1 is preferred over Model 2 [58]. In Bayesian inferences, the numerical evaluation of the evidence is difficult, so estimation methods are opted for, such as thermodynamic integration and steppingstone sampling [59].

The importance of the evidence in model selection in the realm of reflectivity inverse problems has been addressed [60,61]. NS has been applied recently to infer information from XRR data [62,63], also from neutron reflectometry (NR) data [64,65]. NS is used here to examine another statistical probe when determining optical constants using ADR in the EUV spectral range. There are multiple levels of Bayesian inferences. The first level is when a single model is assumed uncontested; the second level is when there are multiple competing models to be sampled [66]. The inferences problem here is considered of the first level. Arguably, the uncontested model here is constructed with the aid of complementary XRR measurements. XRR data are known for their potential to define a structural model with a minimally assumptive manner when analyzed using frequency analysis [67]. Yet, additional complementary measurements are not always available or even feasible when determining optical constants from EUVR data; in such cases, NS would be even of a greater merit.

NS is not exploited in its full capacity here, as in no Bayesian model selection is conducted based on the evidence. Still, this report is highly relevant for enhancing optical constants determination schemes from EUVR data. In addition to the indicated, general, advantages in the introduction of NS over MCMC methods, in some cases, NS has even higher efficiency in achieving the presumed convergence.

4. INVERSE PROBLEM ADJUSTMENT AND DATA ANALYSIS

Determining optical constants via ADR requires solving an inverse problem. To better initialize a model for the samples and to verify the realization of the targeted structures, the XRR profiles measured at Cu−Kα energy were analyzed using the fast Fourier transform (FFT) formalism (Fig. 1) [68,69]. The benefits of using the FFT for XRR analysis are well known [70,71]. The FFT spectrum ideally shows the interfacial depths within a stratification from which separate layers' thicknesses could be inferred [70]. The interpolated FFT profiles shown in Fig. 1 were calculated using the Poust *et al*. method [72].

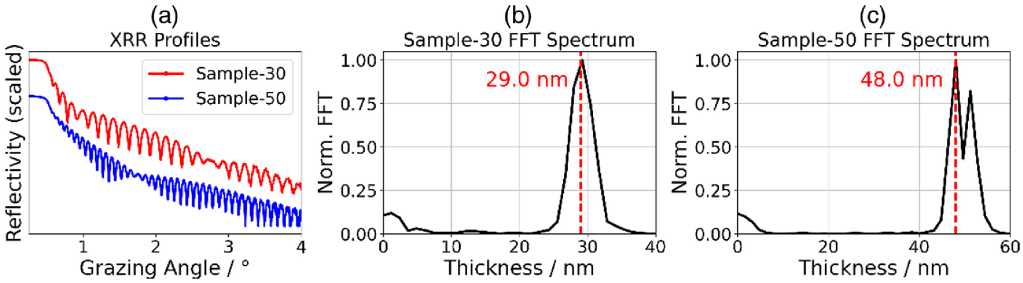

Fig. 1. Frequency analysis of the XRR profiles collected from Sample 30 and a twin sample of Sample 50. (a) Collected XRR profiles from the two samples. Data are scaled for better visibility. (b) Normalized FFT of Sample 30 XRR profile. Vertical red line marks the peak at ca. 29.0 nm. (c) Normalized FFT of an XRR profile for the twin of Sample 50. Line marks one peak at ca. 48.0 nm.

The marked peaks [Figs. 1(b) and (c)] from the FTT spectra of the XRR profiles collected from Sample 30 and the twin of Sample 50 indicate good agreement with the depositions' nominal settings. The attained thicknesses are less than 5% off the targeted.

The peak regarding the spectrum of the twin of Sample 50 [Fig. 1(c)] above 50.0 nm could indicate the presence of another layer. Presumably, a surface layer on top of the Ta deposition is due to oxidation and contamination. Ta thin films' oxidation has been extensively investigated [73,74]. Concerning previous work of ours, x-ray photoelectron spectroscopy (XPS) measurements on a Ta thin film revealed the presence of an oxide layer [20]. Therefore, modeling an oxide layer with the stoichiometry of Ta_2O_5 can be assumed. No evident second peak was observed in the FTT spectrum regarding Sample 30; one possible cause for that is the preparatory processing carried on the experimental data prior to calculating the FTT spectrum. The experimental data were interpolated, differentiated, and further windowed. There could be other reasons, too. However, in order to include the side effects of the physiosorbed and chemisorbed hydrocarbons and other contaminants that are known to build up on optical surfaces, a third layer is also assumed. Oxidation and contamination layers are not sharply bounded and well-defined but rather intermixed and nonstoichiometric [36]. With the argument elaborated in our earlier work considering the optical constants of Ru [36], oxidation and contamination are modeled as two discrete layers since modeling nonuniform profiles (gradients) is computationally laborious and time-consuming [75]. Optimally, a more realistic approach with a gradient profile is intuitively favored. However, the computational prerequisites make a more realistic modeling prohibitive here, given the large number of EUVR profiles, especially since we adopt a global optimization strategy [13,36]. Summing up, for modeling the two samples we assume a trilayer stratification consisting of a carbonaceous contamination layer, an oxidation layer followed by the main Ta deposition on top of the Si substrate.

When determining the optical constants from ADR, the two components of the complex index of refraction δ and β are left as free parameters. Seventy-seven EUVR scans were taken between 5.0 and 24.0 nm for Sample 30; 41 scans were taken between 10.0 and 20.0 nm for Sample 50. Regarding Sample 30, if all of the optical constants of the addressed trilayer stratification with the structure's characteristics would be included in array $\mathbf{p}$, then more than 600 parameters are to be sampled. Such a large number of free parameters in a problem must be avoided. Bellmann coined the term "curse of dimensionality" to indicate a number of overwhelming issues ascribed with highly dimensional optimization problems [36,76,77]. Therefore, the optical constants of the substrate and those of C are to be taken from the Center for X-Ray Optics (CXRO) database [45]. Additionally, given the anticipated vulnerability of the optical response of the samples to the correlations between the optical constants of Ta and its oxide, the independent-atom approximation (IAA) is to be used (Fig. 2) [45,36]:

$$\bar{n}(\lambda) = 1 - \delta(\lambda) + i\beta(\lambda) = 1 - \frac{r_e}{2\pi}\lambda^2 \sum_{j=1}^{N} k_j \, f(\lambda)_j \,. \quad \textbf{(9)}$$

Here, r_e denotes the classical electron radius, λ stands for the wavelength, and k is the number of atoms of type j per unit volume; $f(\lambda)_j$ is the complex atomic scattering factor (ASF) for an atom of type j and is given as:

$$f(\lambda) = f_1(\lambda) - i\, f_2(\lambda) \,, \quad \textbf{(10)}$$

where f_1 relates to the dispersion and f_2 relates to the absorption and an interacting electromagnetic wave.

The formalism now is to sample the ASFs of Ta, the density of the (assumed) oxidation layer in addition to the structural characteristics of the models. The ASFs of O are needed to enable the IAA approach for decreasing the dimensionality of the problem; they are fixed in our calculations from the CXRO database [45]. The simulated reflectivity is produced using Parratt's recursive formalism coupled with Névot–Croce factors to consider the effects of interfacial imperfections [78–80]. Névot–Croce factors are known for including the effects from interfacial roughness and interdiffusion. Interfacial roughness induces off-specular scattering, and interdiffusion reduces the optical contrast for an interface, which increases its transmissivity [81]. Both imperfection types are indistinguishable, given our collected EUVR data, since they both cause the damping of the measured (specular) signal. Hence, the potential interdiffusion between Ta and the Si substrate is modeled here using Névot–Croce factors. Additionally, the absolute weighted uncertainties of the likelihood were expanded with an additional linear contribution as the following [36,82,83]:

$$\sigma^2 = {\sigma_{\text{experimental}}}^2 + \left(a \cdot R_{\text{simulated},\, n}\right)^2 + b^2. \quad \textbf{(11)}$$

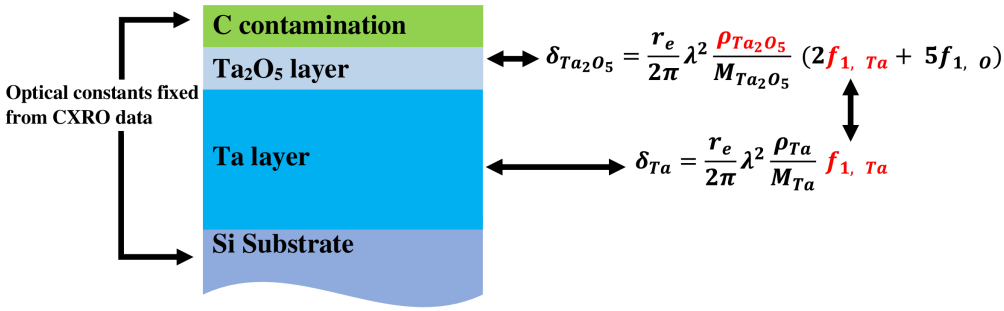

Fig. 2. Sketch of the assumed trilayer stratification of the samples with the corresponding IAA taken for the inverse problem and demonstrated for the refractive indices of Ta and Ta_2O_5. Red-marked parameters are those left free.

Table 1. Comparison of Selected Parameters Relevant to the (Assumed) Structures of the Two Samples as Retrieved from the EUVR Data Using the Addressed NS Bayesian Inferences Approach

	Sample	
Parameter	**Sample 30**	**Sample 50**
C, layer thickness/nm	1.326(22)	1.468(43)
Ta_2O_5, layer thickness/nm	2.4369(61)	2.135(37)
Ta, layer thickness/nm	28.334(12)	47.068(32)
Ta_2O_5, layer density/g/ cm^3	8.568(18)	8.316(90)

This expanded error modeling is effective in compensating the trilayer stratification's deficiencies in describing the intricate subtleties of the real thin film structure. The so-called "discrete-layer approach" is used here, which assumes perfectly uniform vertical and lateral homogeneities for each layer [13]. Relevant to the aforementioned discussion, it is improbable that all layers possess a perfect and unvarying stoichiometric structure. The addressed error modeling and the IAA adaptation to decrease the problems' dimensionalities have been presented and tested in a previous work of ours concerning the determination of Ru optical constants [36]. To this end, to enable Bayesian inferences, the inverse-problem was sampled using the Python implementation of NS DYNESTY [38,84–86].

For the ASFs of Ta, the inferences' priors were initialized based on Henke's tabulations of 1993 [45]. The density for the two Ta depositions were assumed at $16.4\ g/cm^3$, equal to the bulk density [87]. Each of the two EUVR data sets were sampled independently, but the inferences were conducted globally for the entire spectral range, which was measured from each sample. The sampling resumed until meeting the default stopping criterion of the used NS implementation [38]. Upon assuming convergence attainment, the sampled prior modes were integrated. The structural characteristics seem credible; the simulated thicknesses of the Ta deposition for the two samples (Table 1) agree with the results of the FT spectra. The oxides' densities are also close to the experimentally reported value of $8.7\ g/cm^3$ for tantalum oxide [73], though in [73] a specific stoichiometry was not assumed.

For the two samples, the surface layers known to have built-up grew under uncontrolled environments. The two samples were not exposed to the exact identical conditions, either. The effects of these buildups were modeled using the (assumed) two uppermost layers. Hence, differences in the characteristics of these two layers are not surprising. Additionally, atomic force microscopy (AFM) images collected from similar samples to Sample 30 and Sample 50 showed different surface roughness [20,21]. That is also expected since crystallization of a thin film is related to its thickness. The grain sizes in the two samples are expected to be different, ultimately affecting the surface roughness, which influences the sticking probability of volatile contaminates. The correlation between surface roughness and thickness in metallic thin films has been reported before [88,89].

5. DETERMINED OPTICAL CONSTANTS AND SIMULATED EUVR

All the retrieved ASFs from the EUVR data collected from the two samples exhibit Gaussian profiles, with clear cross-correlations with the structural parameters. The uncertainty of each parameter is defined as the confidence interval (CI) of $3-\sigma$. The cross-correlations with the layers' thicknesses and the covariances of two selected ASF retrieved from Samples 30 are shown in Fig. 3.

Although the ASFs were initialized for the sampling process around those from 1993 of Henke (the old CXRO data set) [45], the optical constants profiles for both δ and β converged to a relatively closer agreement with updated values of the CXRO (Fig. 4) [45,92]. The (minimal) prior region is shown in Fig. 4. Our optical constants profiles show noticeable contradictions with those updated values from the CXRO [45,92] for δ above ca. 22 nm and regarding β above ca. 20 nm. Generally, our results contradict the reported optical constants by Windt *et al.* [47] and Palik [46], in addition to those calculated by Chantler [49].

An interesting finding scrutinizing Fig. 4 is the inequality, in some ranges, between the optical constants retrieved from Sample 30 and Sample 50. The uncertainty bands are plotted for two selected spectral segments, to better compare the optical constants retrieved from the two samples in Fig. 5. These inequalities can be attributed to numerous causes. At a first glance, one might assume the cause to be the dissimilarity in the probed spectral ranges of the two samples, as in the anticipated influence of including scans at shorter wavelengths regarding Sample 30. Thus, one could argue that this provides higher sensitivity to some structural characteristics, which consequently alter the retrieved optical constants. However, determining the optical constants from Sample 30 merely taking the spectral

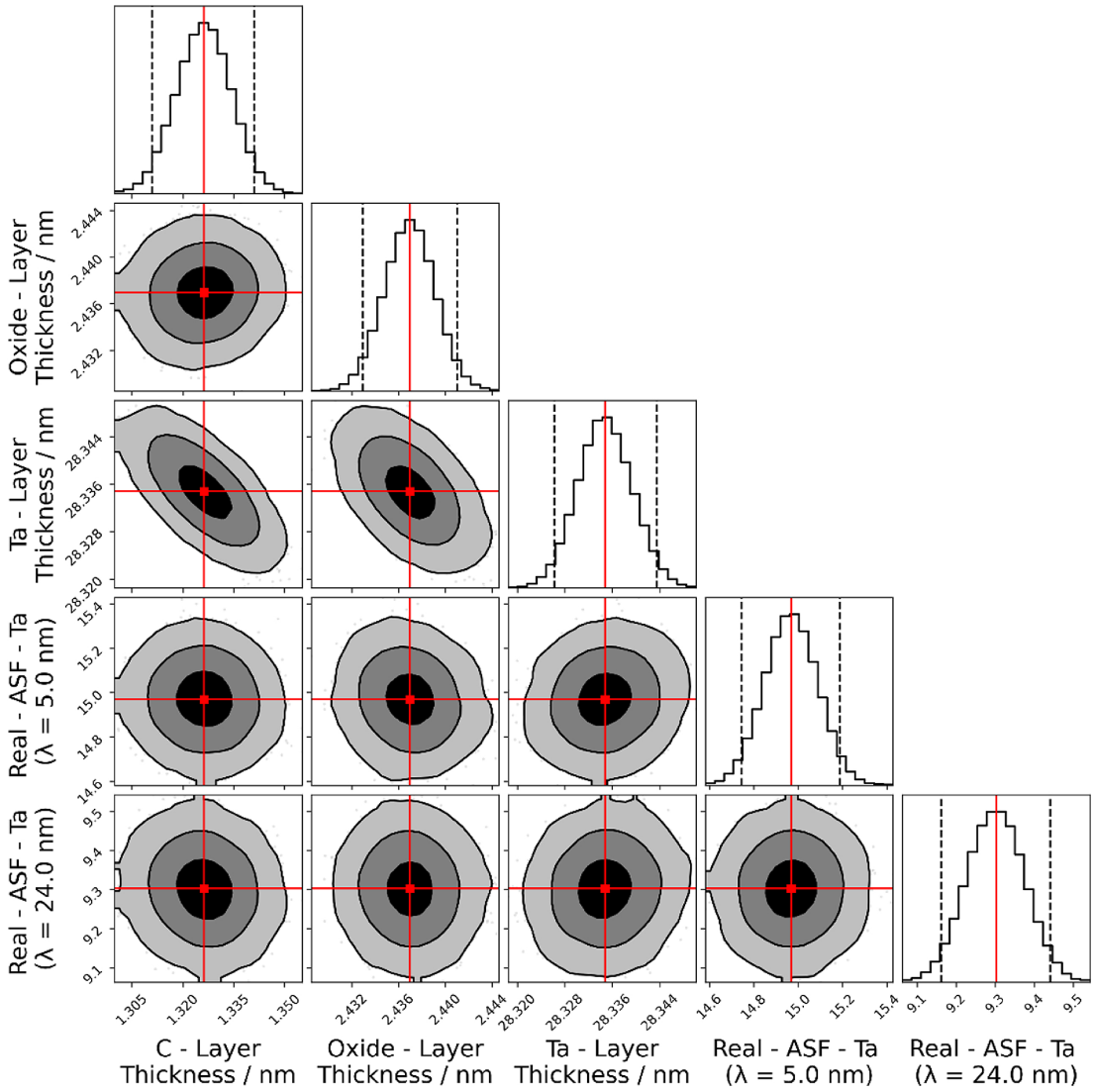

Fig. 3. Posterior distributions projected regarding five selected parameters retrieved from Sample 30 EUVR measurements. Fitted 1D histograms modes are marked by red lines. Dashed black lines confine the CI of $3-\sigma$. Contour plots of the 2D histograms show the 1, 2, and $3-\sigma$ density regions [90,91].

range 10.0–20.0 nm has been tried, and the inequalities subsist. With that in mind, the following discussion will focus on three relevant aspects attempting to explain the addressed inequalities: sample specifics; thickness correlation; and modeling subtilties.

Beginning with sample specifics, generally, it is well known that the optical constants of a thin film depend on its morphology [94,95]. Recently, Sinha *et al*. demonstrated the correlation between the optical constants of zirconium-oxide thin films and their morphologies in the 500–560 eV energy range [95]. It could be that there are *slight* differences in the morphologies between the Ta depositions of Sample 30 and Sample 50. X-ray diffraction data collected from similar samples in Sample 30 and Sample 50 showed similar diffractograms [20,21], which could indicate an equal phase distribution but does not mean identical morphologies regarding the two depositions of Sample 30 and Sample 50. The crystallization is expected to be different, given the different thickness (as discussed in Section 4). Residual traces of the sputtering gas might also play a role. The scenario for the two Ta samples to have other morphological disparities can only be excluded with additional parametric comparative studies.

The second aspect is thickness correlation. Regarding thin films, there are numerous reports claiming results retrieved from experimental data that demonstrate a dependence of optical constants on the thickness, e.g., Ag thin films in the visible light range [96]. A few reports also exist regarding the EUV and the soft x-ray spectral ranges. For instance, the optical constants of Au thin films, in the words of Yanagihara *et al*. [97], "show definite dependence" on the thickness. Yanagihara *et al*. investigated the energy range from 60 to 900 eV and found no clear difference regarding Au phases regarding the different samples investigated; yet, they indicated that further investigation of the phases is needed [97].

Concerning the third aspect, modeling subtilties, for instance, the two samples were modeled with an oxide layer

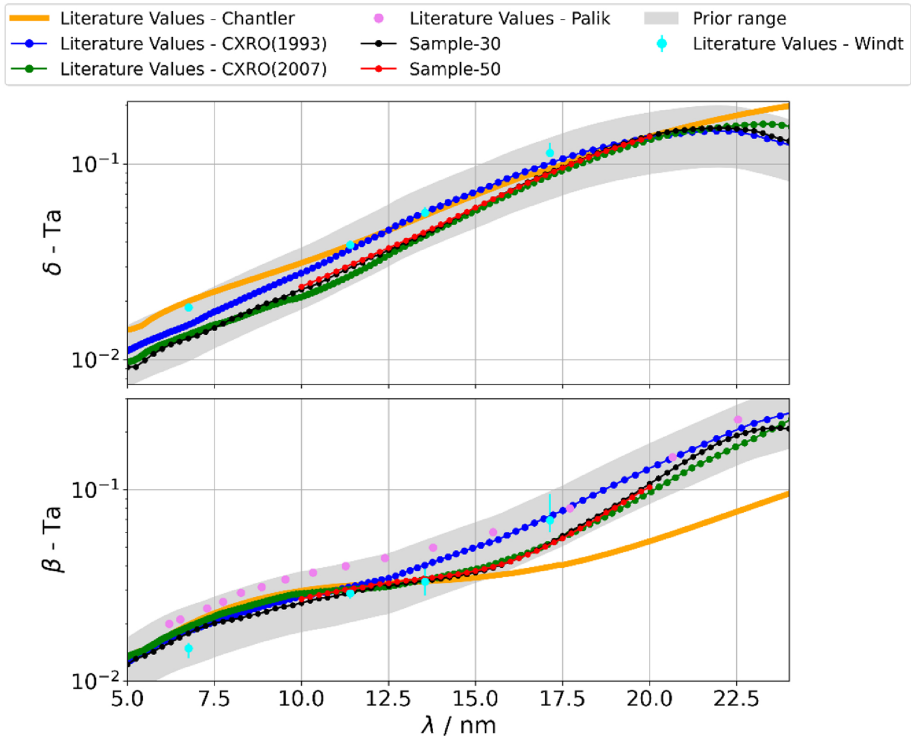

Fig. 4. Calculated optical constants of Ta in our work for the two samples, with comparison to other literature data regarding the spectral range 5.0–24.0 nm [45–50,92,93]. The vertical axes are log-scaled. Top: Profiles of the refractive indices. Bottom: Profiles of the extinction coefficients.

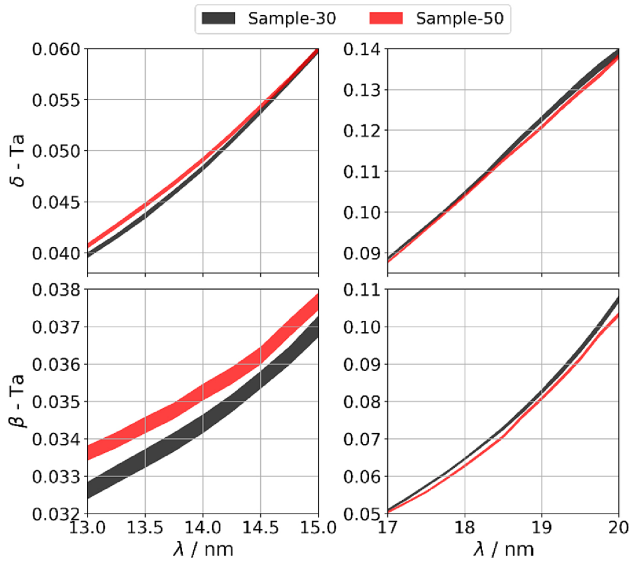

Fig. 5. Retrieved profiles of the optical constants from the two samples compared regarding two selected spectral segments; 13.0–15.0 and 17.0–20.0 nm. Curves show interpolated profiles considering the calculated CI of $3-\sigma$.

with the same stoichiometry, a plausible assumption but cannot be acclaimed unequivocal. There could be slight differences in the oxidation stoichiometries, however. Similarly, the tri-layer model itself is a simplified one. The simulated EUVR was assumed as perfectly S -polarized, and the interfacial imperfections were assumed to have a Gaussian distribution. The latter assumption is made by default since Névot–Croce factors were used [80]. The discussion given in Section 4 is pertinent to this direction. The uncertainties in the angles' values were not included. Also, the optical constants of the substrate and other materials were fixed in the sampling process. It is not known exactly here how the systematic errors in the values of the referenced data sets had affected the sampled parameters. Although the superficial contamination was considered in the model, which is quite critical in the EUV range, only elemental C layers were considered. Contamination usually contains residual process gases, i.e., adsorbed water from air moisture among other *peculiarities*. On the other hand, including a fitting parameter for every single detail is not an option. Tractability plays a role here, which is the viability of attaining an expected convergence for an inverse problem given tenable conditions [55]. Constructing an inverse problem with an overwhelming number of free parameters would aggravate the curse of dimensionality and, in most cases, yield an intractable problem. Here, a settlement is made between the curse of dimensionality and tractability via simplified but sound models for the samples. When determining optical constants using ADR, side effects concomitant to the assumptions made to maintain the tractability are expected. Consequently, that could be another reason behind the observed inequalities in the determined optical constants from the two samples.

Nevertheless, the retrieved optical constants from the two samples are not colossally different. In some segments, their uncertainty ranges partially overlap (Fig. 5). This supports our uncertainty estimation being realistic. Also, the simulated EUVR maps are close to the measured ones; the maps regarding Sample 30 are as shown (Fig. 6). The highest residuals are

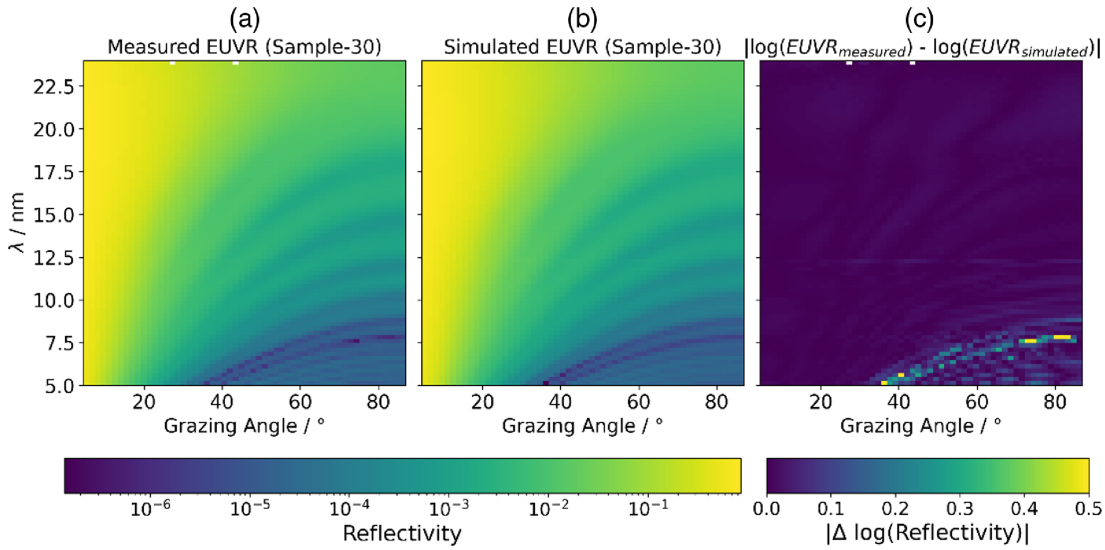

Fig. 6. Demonstration for the goodness-of-fit achieved by the NS algorithm. (a) Measured data, the two white points at the wavelength of 24.0 nm are two masked corrupted values. (b) Simulated EUVR map. (c) Absolute of the logarithm of the residual between the measurements and the simulation.

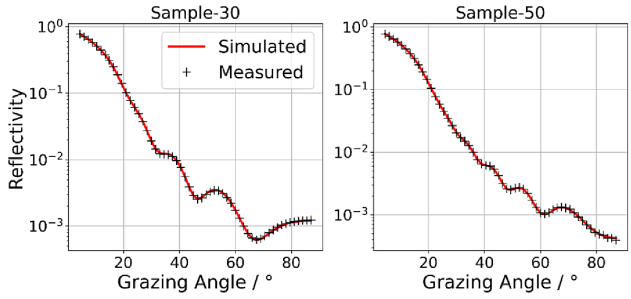

Fig. 7. Plotting of the measured data and its simulation regarding the two samples for the wavelength of 13.5 nm.

observed in the high-energy–high-grazing angular region [Fig. 6(c)], where Kiessig fringes (see [98]) are most prominent. This can be explained by the high-sensitivity of modeling Kiessig fringes to the assumed structure. The high-energy–high-grazing angular region indicates information about the sample, given the highest penetration depth. Hence, this region is the most sensitive, in comparison with other data collected here, to use the model's deficiencies [36].

To better reveal the goodness-of-fit achieved by the NS algorithm, the measured and the simulated EUVR profiles regarding a wavelength of 13.5 nm are plotted (Fig. 7).

Although the divergence of the incident beam was not modeled, most Kiessig fringes' features were well simulated. Moreover, the presented results here are to be understood as strictly valid for the described tetralayer models. For example, the optical constants of the (assumed) carbonaceous layer were taken from the CXRO database [45]; if the optical constants were taken from a different source, the retrieved optical constants of Ta will be slightly different. That is a corollary when treating such an inverse problem.

6. CONCLUSIONS AND PERSPECTIVES

We have determined the optical constants of Ta with the corresponding uncertainties in the spectral range 5.0–24.0 nm from EUVR measurements. Our results were compared with external literature values and found close to those updated values of the CXRO database ([45]). We have also reviewed three aspects relevant to addressing the discrepancies regarding different optical constants data sets, concerning the same material. It seems that the optical constants of real samples can hardly be described as universal optical parameters [95]. The review of this report ascribes this dilemma to the probed samples' specifics, contamination, impurities, interface imperfections, and modeling subtilties. In the EUV range, generally, it is not uncommon to report slightly different optical constants for the same material in a report. Maehara *et al*. [99] reported slightly different optical constants for Pt and Rh thin films upon determining them using ADR and the photoelectric yield measurements from the same samples. Schlegel also showed different optical constants of Ru regarding ADR and TMMs [100].

The applicability of an NS algorithm is successfully tested here. NS is a known statistical approach for gleaning valuable information in inverse problems and, in some situations, could also provide higher efficiency than that of MCMC algorithms. The estimated evidence was not used for model selection, since this would require simulating multiple models to enable estimating the BF [see Eq. (8)]. Nevertheless, the models were selected based on the FFT analysis of the XRR profiles; further, the estimated evidence was (partly) incorporated to address a stopping criterion for the simulations here. Additional details on how the estimated evidence is incorporated for the realization of a stopping criterion are available in [38]. This report is a step further in developing ADR for determining optical constants in the EUV range, where estimating the evidence is valuable for model selection, especially when no complementary data are available.

Nevertheless, we do not present NS as better than any other Bayesian inferences or even other optimization methods (see [38]). Benchmarking such methods requires test problems and is laborious [101]. When comparing two computational approaches, many technical features have to be scrutinized, parallelization efficiency and user friendliness are such two. Benchmarking NS is outside the context here. A comparison between NS and other inferences methods was made by Allison and Dunkley [102].

The results here are pertinent to further develop EUVL technology, particularly when assessing the applicability of Ta as an absorber layer constituent.

The optical constants of Ta are available on the PTB's online Optical Constants Database (www.ocdb.ptb.de/home).

Funding. Electronic Components and Systems for European Leadership (783247); European Metrology Programme for Innovation and Research (20IND04).

Acknowledgment. This project has received funding from the Electronic Component Systems for European Leadership Joint Undertaking (Technology Advances for Pilot Line of Enhanced Semiconductors for 3 nm) and from the EMPIR Metrology for Industry Project, i.e., traceable metrology of soft x-ray to IR optical constants and nanofilms for advanced manufacturing (ATMOC). This joint undertaking receives support from the European Union's Horizon 2020 research and innovation program alongside Netherlands, Belgium, Germany, France, Austria, United Kingdom, Israel, and Switzerland.

Disclosures. The authors declare no conflicts of interest.

Data availability. The EUVR data underlying the optical constants results presented in this paper are available in [103]. The XRR data underlying the FFT results presented in this paper are not publicly available at this time but may be obtained from the authors upon reasonable request.

REFERENCES

1. ASML WWW site, "Stories section," https://www.asml.com/en/news/stories/2022/making-euv-lab-to-fab.
2. M. van de Kerkhof, H. Jasper, L. Levasier, R. Peeters, R. van Es, J.-W. Bosker, A. Zdravkov, E. Lenderink, F. Evangelista, P. Broman, B. Bilski, and T. Last, "Enabling sub-10 nm node lithography: Presenting the NXE:3400B EUV scanner," Proc. SPIE **10143**, 101430D (2017).
3. N. Mojarad, J. Gobrecht, and Y. Ekinci, "Beyond EUV lithography: A comparative study of efficient photoresists' performance," Sci. Rep. **5**, 9235 (2015).
4. P. Uzoma, S. Shabbir, H. Hu, P. Okonkwo, and O. Penkov, "Multilayer reflective coatings for BEUV lithography: A review," Nanomaterials **11**, 2782 (2021).
5. S. Hong, J. Kim, J. Lee, S. Lee, J. Kim, and J. Ahn, "Evaluation of metal absorber materials for beyond extreme ultraviolet lithography," J. Nanosci. Nanotechnol. **15**, 8652–8655 (2015).
6. J. Lean, T. Woods, F. Eparvier, R. Meier, D. Strickland, J. Correira, and J. Evans, "Solar extreme ultraviolet irradiance: Present, past, and future," J. Geophys. Res. **116**, A01102 (2011).
7. R. Arita, T. Nakazato, T. Shimizu, K. Yamanoi, M. Empizo, T. Hori, K. Fukuda, Y. Minami, N. Sarukura, M. Tanaka, M. Nishikino, and T. Fukuda, "High spatial resolution ZnO scintillator for an in situ imaging device in EUV region," Opt. Mater. **36**, 2012–2015 (2014).
8. L. Juschkin, R. Freiberger, and K. Bergmann, "EUV microscopy for defect inspection by dark-field mapping and zone plate zooming," J. Phys. Conf. Ser. **186**, 012030 (2009).
9. W. Eschen, L. Loetgering, V. Schuster, R. Klas, A. Kirsche, L. Berthold, M. Steinert, T. Pertsch, H. Gross, M. Krause, J. Limpert, and J. Rothhardt, "Material-specific high-resolution table-top extreme ultraviolet microscopy," Light Sci. Appl. **11**, 117 (2022).
10. L. Loetgering, S. Witte, and J. Rothhardt, "Advances in laboratory-scale ptychography using high harmonic sources," Opt. Express **30**, 4133–4164 (2022).
11. I. Ul Ahad, M. Obeidi, B. Budner, A. Bartnik, H. Fiedorowicz, and D. Brabazon, "Surface roughness control by extreme ultraviolet (EUV) radiation," AIP Conf. Proc. **1896**, 200008 (2017).
12. N. Pauly, F. Yubero, and S. Tougaard, "Optical properties of molybdenum in the ultraviolet and extreme ultraviolet by reflection electron energy loss spectroscopy," Appl. Opt. **59**, 4527–4532 (2020).
13. Q. Saadeh, P. Naujok, D. Thakare, M. Wu, V. Philipsen, F. Scholze, C. Buchholz, Z. Salami, Y. Abdulhadi, D. García, H. Mentzel, A. Babuschkin, C. Laubis, and V. Soltwisch, "On the optical constants of cobalt in the M-absorption edge region," Optik, submitted for publication.
14. J. Rebellato, E. Meltchakov, R. Soufli, S. De Rossi, X. Zhang, F. Auchère, and F. Delmotte, "Analyses of tabulated optical constants for thin films in the EUV range and application to solar physics multilayer coatings," Proc. SPIE **10691**, 106911U (2018).
15. R. Soufli, F. Delmotte, J. Meyer-Ilse, F. Salmassi, N. Brejnholt, S. Massahi, D. Girou, F. Christensen, and E. Gullikson, "Optical constants of magnetron sputtered Pt thin films with improved accuracy in the N- and O-electronic shell absorption regions," J. Appl. Phys. **125**, 085106 (2019).
16. J. Seely, L. Goray, D. Windt, B. Kjornrattanawanich, Y. Uspenskii, and A. Vinogradov, "Extreme ultraviolet optical constants for the design and fabrication of multilayer-coated gratings," Proc. SPIE **5538**, 43–52 (2004).
17. V. Bakshi, *EUV Lithography*, 2nd ed., SPIE Monographs (2018), Chap. 7.
18. T. Yoshihara, S. Kotsuji, and K. Suzuki, "Sputtered TaX film properties for x-ray mask absorbers," J. Vac. Sci. Technol. B **14**, 4363 (1996).
19. H. Kang, P. Peranantham, C. Hwangbo, H.-S. Seo, S.-S. Kim, and J. Lee, "Optical properties of $TaTe_2O_7$ thin films as absorber materials for extreme ultraviolet lithography binary masks," J. Vac. Sci. Technol. B **30**, 06F505 (2012).
20. M. Wu, J. de Marneffe, K. Opsomer, C. Detavernier, A. Delabie, P. Naujok, Ö. Caner, A. Goodyear, M. Cooke, Q. Saadeh, V. Soltwisch, F. Scholze, and V. Philipsen, "Characterization of Ru4-xTax (x = 1,2,3) alloy as material candidate for EUV low-n mask," Micro Nano Eng. **12**, 100089 (2021).
21. D. Thakare, M. Wu, K. Opsomer, C. Detavernier, P. Naujok, Q. Saadeh, V. Soltwisch, A. Delabie, and V. Philipsen, "Evaluation of Ta-Co alloys as novel high-k EUV mask absorber," Proc. SPIE **12051**, 120510D (2022).
22. B. Da, Y. Sun, S. F. Mao, Z. M. Zhang, H. Jin, H. Yoshikawa, S. Tanuma, and Z. J. Ding, "A reverse Monte Carlo method for deriving optical constants of solids from reflection electron energy-loss spectroscopy spectra," J. Appl. Phys. **113**, 214303 (2013).
23. K. Rosfjord, C. Chang, R. Miyakawa, H. Barth, and D. Attwood, "Direct index of refraction measurements at extreme-ultraviolet and soft-x-ray wavelengths," Appl. Opt. **45**, 1730–1736 (2006).
24. L. Seve, J.-M. Tonnerre, and D. Raoux, "Determination of the anomalous scattering factors in the soft-x-ray range using diffraction from a multilayer," J. Appl. Cryst. **31**, 700–707 (1998).
25. W. Hunter, "Measurement of optical properties of materials in the vacuum ultraviolet spectral region," Appl. Opt. **21**, 2103–2114 (1982).
26. R. Soufli, "Optical constants of materials in the EUV/soft x-ray region for multilayer mirror applications," Ph.D. thesis (University of California, 1997).
27. W. Hunter, "Measuring optical constants from the UV to x-ray wavelengths: how it was (and is) done," Proc. SPIE **5538**, 1–16 (2004).
28. E. Spiller, *Soft X-Ray Optics* (SPIE, 1994), Chap. 2.
29. J. Larruquert, *Optical Thin Films and Coatings from Materials to Applications*, 2nd ed. (Elsevier, 2018), Chap. 7.
30. D. Attwood, G. Sommargren, R. Beguiristain, K. Nguyen, J. Bokor, N. Ceglio, K. Jackson, M. Koike, and J. Underwood, "Undulator radiation for at-wavelength interferometry of optics for extreme-ultraviolet lithography," Appl. Opt. **32**, 7022–7031 (1993).

31. M. Hobson and J. Baldwin, "Markov-chain Monte Carlo approach to the design of multilayer thin-film optical coatings," Appl. Opt. **43**, 2651–2660 (2004).
32. F. Feroz and M. Hobson, "Multimodal nested sampling: an efficient and robust alternative to Markov chain Monte Carlo methods for astronomical data analyses," Mon. Not. R. Astron. Soc. **384**, 449–463 (2008).
33. R. van de Schoot, S. Depaoli, R. King, B. Kramer, K. Märtens, M. Tadesse, M. Vannucci, A. Gelman, D. Veen, J. Willemsen, and C. Yau, "Bayesian statistics and modelling," Nat. Rev. Methods Primers **1**, 1 (2021).
34. A. Gottwald, K. Wiese, U. Kroth, and M. Richter, "Uncertainty analysis for the determination of B4C optical constants by angle-dependent reflectance measurement for 40 nm to 80 nm wavelength," Appl. Opt. **56**, 5768–5774 (2017).
35. A. Gottwald, K. Wiese, T. Siefke, and M. Richter, "Validation of thin film TiO_2 optical constants by reflectometry and ellipsometry in the VUV spectral range," Meas. Sci. Technol. **30**, 045201 (2019).
36. Q. Saadeh, P. Naujok, V. Philipsen, P. Hönicke, C. Laubis, C. Buchholz, A. Andrle, C. Stadelhoff, H. Mentzel, A. Schönstedt, V. Soltwisch, and F. Scholze, "Time-frequency analysis assisted determination of ruthenium optical constants in the sub-EUV spectral range 8 nm–23.75 nm," Opt. Express **29**, 40993–41013 (2021).
37. J. Skilling, "Nested Sampling," AIP Conf. Proc. **735**, 395 (2004).
38. J. Speagle, "DYNESTY: a dynamic nested sampling package for estimating Bayesian posteriors and evidences," Mon. Not. R. Astron. Soc. **493**, 3132–3158 (2020).
39. M. Cowles and B. Carlin, "Markov chain Monte Carlo convergence diagnostics: A comparative review," J. Am. Stat. Assoc. **91**, 883–904 (1996).
40. F. Feroz and J. Skilling, "Exploring multi-modal distributions with nested sampling," AIP Conf. Proc. **1553**, 106 (2013).
41. K. Kusumo, L. Gomoescu, R. Paulen, S. Muñoz, C. Pantelides, N. Shah, and B. Chachuat, "Bayesian approach to probabilistic design space characterization: a nested sampling strategy," Ind. Eng. Chem. Res. **59**, 2396–2408 (2020).
42. L. Pártay and G. Hantal, "Stability of the high-density Jagla liquid in 2D: sensitivity to parameterisation," Soft Matter **18**, 5261–5270 (2022).
43. D. Huijser, "Bayesian statistics in astronomy," Ph.D. thesis (The University of Auckland, 2020).
44. M. Hosoya, N. Sakaya, O. Nozawa, Y. Shiota, K. Hamamoto, O. Nagarekawa, S. Shimojima, T. Shoki, T. Watanabe, and H. Kinoshita, "Evaluating the optical index of Ta and Ta-based absorbers for an extreme ultraviolet mask using extreme ultraviolet reflectometry," Jpn. J. Appl. Phys. **47**, 4898–4905 (2008).
45. B. Henke, E. Gullikson, and J. Davis, "X-Ray interactions: photoabsorption, scattering, transmission, and reflection at E = 50-30,000 eV, Z = 1-92," At. Data Nucl. Data Tables **54**, 181–342 (1993).
46. Updates to the tabulated value are accessible in the CXRO online database via: https://henke.lbl.gov/optical_constants/asf.html.
47. E. Palik, *Handbook of Optical Constants of Solids* (Academic, 1998), Vol. **2**.
48. D. Windt, W. Cash, M. Scott, P. Arendt, B. Newnam, R. Fisher, and A. Swartzlander, "Optical constants for thin films of Ti, Zr, Nb, Mo, Ru, Rh, Pd, Ag, Hf, Ta, W, Re, Ir, Os, Pt, and Au from 24 Å to 1216 Å," Appl. Opt. **27**, 246–278 (1988).
49. R. Ciesielski, Q. Saadeh, V. Philipsen, K. Opsomer, J.-P. Soulié, M. Wu, P. Naujok, R. van de Kruijs, C. Detavernier, M. Kolbe, F. Scholze, and V. Soltwisch, "Determination of optical constants of thin films in the EUV," Appl. Opt. **61**, 2060–2078 (2022).
50. C. Chantler, "Theoretical form factor, attenuation, and scattering tabulation for Z = 1–92 from E = 1–10 eV to E = 0.4–1.0 MeV," J. Phys. Chem. Ref. Data **24**, 71–642 (1995).
51. S. Yulin, "Multilayer coatings for EUV/soft x-ray mirrors," in *Optical Interference Coatings*, N. Kaiser and H. Pulker eds., Vol. **88** of Springer Series in Optical Science (Springer-Verlag, 2003).
52. F. Scholze, B. Beckhoff, G. Brandt, R. Fliegauf, A. Gottwald, R. Klein, B. Meyer, U. Schwarz, R. Thornagel, J. Tuemmler, K. Vogel, J. Weser, and G. Ulm, "High-accuracy EUV metrology of PTB using synchrotron radiation," Proc. SPIE **4344**, 402–413 (2001).
53. C. Laubis, A. Kampe, C. Buchholz, A. Fischer, J. Puls, C. Stadelhoff, and F. Scholze, "Characterization of the polarization properties of PTB's EUV reflectometry system," Proc. SPIE **7636**, 76362R (2010).
54. M. Richter and G. Ulm, "Metrology with synchrotron radiation–a brief introduction," PTB-Mitteilungen **124**, 3–6 (2004).
55. G. Ashton, N. Bernstein, J. Buchner, *et al.*, "Nested sampling for physical scientists," Nat. Rev. Methods Primers **2**, 38 (2022).
56. R. Johnson, P. Kirk, and M. Stumpf, "SYSBIONS: nested sampling for systems biology," Bioinformations **31**, 604–605 (2015).
57. C. Pooley and G. Marion, "Bayesian model evidence as a practical alternative to deviance information criterion," R. Soc. Open Sci. **5**, 171519 (2018).
58. N. Friel and J. Wyse, "Estimating the evidence–a review," Stat. Neer. **66**, 288–308 (2012).
59. J. Annis, N. Evans, J. Miller, and T. Palmeri, "Thermodynamic Integration and Steppingstone sampling methods for estimating Bayes factors: A tutorial," J. Math. Psychol. **89**, 67–86 (2019).
60. D. Sivia, W. David, K. Knight, and S. Gull, "An introduction to Bayesian model selection," Physica D **66**, 234–242 (1993).
61. D. Windover, D. Gil, J. Cline, A. Henins, N. Armstrong, P. Hung, S. Song, R. Jammy, and A. Diebold, "X-ray reflectometry determination of structural information from atomic layer deposition nanometer-scale hafnium oxide thin films," MRS Proc. **996**, 705 (2007).
62. T. McCoy, A. Armstrong, J. Moore, S. Holt, R. Tabor, and A. Routh, "Spontaneous surface adsorption of aqueous graphene oxide by synergy with surfactants," Phys. Chem. Chem. Phys. **24**, 797–806 (2022).
63. A. Milsom, A. Squires, M. Skoda, P. Gutfreundd, E. Masonbe, N. Terrill, and C. Pfrang, "The evolution of surface structure during simulated atmospheric ageing of nano-scale coatings of an organic surfactant aerosol proxy," Environ. Sci. Atmos. **2**, 964–977 (2022).
64. A. McCluskey, J. Cooper, T. Arnold, and T. Snow, "A general approach to maximise information density in neutron reflectometry analysis," Mach. Learn. **1**, 035002 (2020).
65. J. Durant, L. Wilkins, K. Butler, and J. Cooper, "Determining the maximum information gain and optimizing experimental design in neutron reflectometry using the Fisher information," J. Appl. Cryst. **54**, 1100–1110 (2021).
66. R. Trotta, "Bayesian methods in cosmology," arXiv:1701.01467 (2017), Ch. 4.
67. K. Sakurai, M. Mizusawa, and M. Ishii, "Significance of frequency analysis in x-ray reflectivity: towards analysis which does not depend too much on models," Trans. Mater. Res. Soc. Jpn. **33**, 523–528 (2008).
68. C. Harris, K. Millman, S. van der Walt, *et al.*, "Array programming with NumPy," Nature **585**, 357–362 (2020).
69. J. Cooley and J. Tukey, "An algorithm for the machine calculation of complex Fourier series," Math. Comput. **19**, 297–301 (1965).
70. F. Bridou and B. Pardo, "Grazing x-ray reflectometry data processing by Fourier transform," J. X-RAY Sci. Technol. **4**, 200–216 (1994).
71. J. Wernecke, A. Shard, and M. Krumrey, "Traceable thickness determination of organic nanolayers by x-ray reflectometry," Surf. Interface Anal. **46**, 911–914 (2014).
72. B. Poust, R. Sandhu, and M. Goorsky, "Multi-layer thickness determination using differential-based enhanced Fourier transforms of x-ray reflectivity data," Phys. Stat. Sol. A **206**, 1780–1784 (2009).
73. P. Yunina, Y. Drozdova, and N. Guseva, "Grazing incidence x-ray diffraction study of tantalum thin films," J. Synch. Investig. **12**, 701–704 (2018).
74. C. Steidel and D. Gerstenberg, "Thermal oxidation of sputtered tantalum thin films between 100° and 525°C," J. Appl. Phys. **40**, 3828 (1969).
75. Y. Esashi, M. Tanksalvala, Z. Zhang, N. Jenkins, H. Kapteyn, and M. Murnane, "Influence of surface and interface roughness on x-ray and extreme ultraviolet reflectance: A comparative numerical study," OSA Contin. **4**, 1497–1518 (2021).
76. R. Bellman, *Dynamic Programming* (Princeton, 1957).
77. L. Chen, "Curse of dimensionality," in *Encyclopedia of Database Systems*, L. Liu and M. T. Özsu, eds. (Springer, 2009).
78. L. Parratt, "Surface studies of solids by total reflection of x-rays," Phys. Rev. **95**, 359–369 (1954).

79. J. Als-Nielsen and D. McMorrow, *Elements of Modern X-ray Physics*, 2nd ed. (Wiley, 2011), Sec. 3.6.
80. L. Névot and P. Croce, "Caractérisation des surfaces par réflexion rasante de rayons X. Application à l'étude du polissage de quelques verres silicates," Rev. Phys. Appl. **15**, 761–779 (1980).
81. P. Naujok, S. Yulin, R. Müller, N. Kaiser, and A. Tünnermann, "Interface characterization in B-based multilayer mirrors for next generation lithography," Thin Solid Films **612**, 414–418 (2016).
82. S. Heidenreich, H. Gross, and M. Bar, "Bayesian approach to the statistical inverse problem of scatterometry: comparison of three surrogate models," Int. J. Uncertain. Quantif. **5**, 511–526 (2015).
83. M.-A. Henn, "Statistical approaches to the inverse problem of scatterometry," Ph.D. thesis (Technische Universität Berlin Fakultät II - Mathematik und Naturwissenschaften, 2013).
84. E. Higson, W. Handley, M. Hobson, and A. Lasenby, "Dynamic nested sampling: an improved algorithm for parameter estimation and evidence calculation," Stat. Comput. **29**, 891–913 (2019).
85. F. Feroz, M. Hobson, and M. Bridges, "MULTINEST: an efficient and robust Bayesian inference tool for cosmology and particle physics," Mon. Not. R. Astron. Soc. **398**, 1601–1614 (2009).
86. S. Koposov, J. Speagle, K. Barbary, *et al.*, "joshspeagle/dynesty: v1.2.3," Zenodo (2022), https://doi.org/10.5281/zenodo.6609296.
87. W. Haynes, ed., *CRC Handbook of Chemistry and Physics*, 95th ed. (CRC Press, 2014), Sect. 4.
88. K. Cai, M. Müllera, J. Bossert, A. Rechtenbach, and K. Jandt, "Surface structure and composition of flat titanium thin films as a function of film thickness and evaporation rate," Appl. Surf. Sci. **250**, 252–267 (2005).
89. Z. Xin, S. Xiao-Hui, and Z. Dian-Lin, "Thickness dependence of grain size and surface roughness for dc magnetron sputtered Au films," Chin. Phys. B **19**, 086802 (2010).
90. D. Foreman-Mackey, "Corner.py: Scatterplot matrices in Python," J. Open Source Software **1**, 24 (2016).
91. J. Hunter, "Matplotlib: A 2D graphics environment," Comput. Sci. Eng. **9**, 90–95 (2007).
92. E. Gullikson, F. Salmassi, A. Aquila, J. Frederico, and S.-J. Park, "Revised optical constants of Tantalum for EUV mask absorber materials," LBNL Report #: LBNL-963E Abs (2008). https://escholarship.org/uc/item/70q2d5p4
93. M. Newville, "The XrayDB Python package," GitHub (2021) [accessed 15 November 2022], https://xraypy.github.io/XrayDB/.
94. G. Scott, "Optical constants of thin-film materials*," J. Opt. Soc. Am. **45**, 176–179 (1955).
95. M. Sinha, A. Singh, R. Gupta, A. Yadav, and M. Modi, "Investigation of soft x-ray optical properties and their correlation with structural characteristics of zirconium oxide thin films," Thin Solid Films **721**, 138552 (2021).
96. X. Sun, R. Hong, H. Hou, Z. Fan, and J. Shao, "Thickness dependence of structure and optical properties of silver films deposited by magnetron sputtering," Thin Solid Films **515**, 6962–6966 (2007).
97. M. Yanagihara, T. Maehara, M. Yamamoto, and T. Namioka, "Thickness dependence of the optical constants of thin Pt, Au, and Rh films in the soft x-ray region," Proc. SPIE **1720**, 246 (1992).
98. H. Kiessig, "Interferenz von Röntgenstrahlen an dünnen Schichten," Ann. Phys. **402**, 769–788 (1931).
99. T. Maehara, M. Yanagihara, M. Yamamoto, and T. Namioka, "Optical constants of very thin Pt and Rh films determined from soft-x-ray reflectance and photoelectric yield measurements," Nuc. Inst. Met. Phys. Res. B **74**, 362–367 (1993).
100. U. Schlegel, "Determination of the optical constants of ruthenium in the EUV and soft x-ray region using synchrotron radiation," Diploma thesis (Technische Fachhochschule Berlin, 2000).
101. V. Beiranvand, W. Hare, and Y. Lucet, "Best practices for comparing optimization algorithms," Optim. Eng. **18**, 815–848 (2017).
102. R. Allison and J. Dunkley, "Comparison of sampling techniques for Bayesian parameter estimation," Mon. Not. R. Astron. Soc. **437**, 3918–3928 (2014).
103. Q. Saadeh, P. Naujok, M. Wu, V. Philipsen, D. Thakare, F. Scholze, C. Buchholz, C. Stadelhoff, T. Wiesner, and V. Soltwisch, "Tantalum thin films EUVR data," Zenodo (2022), https://doi.org/10.5281/zenodo.7181799.